Magnetic evolution and anomalous Wilson transition in diagonal phosphorene nanoribbons driven by strain

2015 Nanotechnology 26 295402

(http://iopscience.iop.org/0957-4484/26/29/295402)

IOP Publishing Nanotechnology
Nanotechnology **26** (2015) 295402 (6pp) doi:10.1088/0957-4484/26/29/295402

Magnetic evolution and anomalous Wilson transition in diagonal phosphorene nanoribbons driven by strain

Shuai Zhang[1], Chong Li[1], Zheng Xiao Guo[1,2], Jun-Hyung Cho[1,3], Wan-Sheng Su[4,5] and Yu Jia[1]

[1] International Laboratory for Quantum Functional Materials of Henan, School of Physics and Engineering, Zhengzhou University, Zhengzhou 450001, People's Republic of China
[2] Department of Chemistry, University College London, London WC1E 6BT, UK
[3] Department of Physics and Research Institute for National Sciences, Hanyang University, 17 Haengdang-Dong, Seongdong-Ku, Seoul 133-791, Korea
[4] National Center for High-Performance Computing, Hsinchu 30076, Taiwan
[5] Department of Physics, National Chung Hsing University, Taichung 40227, Taiwan

E-mail: lichong@zzu.edu.cn and jiayu@zzu.edu.cn

Received 24 April 2015, revised 20 May 2015
Accepted for publication 5 June 2015
Published 2 July 2015

Abstract

Inducing magnetism in phosphorene nanoribbons (PNRs) is critical for practical applications. However, edge reconstruction and Peierls distortion prevent PNRs from becoming highly magnetized. Using first-principles calculations, we find that relaxed oxygen-saturated diagonal-PNRs (O-d-PNRs) realize stable spin-polarized antiferromagnetic (AFM) coupling, and the magnetism is entirely localized at the saturated edges. The AFM state is quite stable under expansive and limited compressive strain. More importantly, not only does the irreversible Wilson transition occur when applying strain, but the nonmagnetic (NM) metal phase (a new ground state) becomes more stable than the AFM state when the compressive strain exceeds −4%. The related stability and transition mechanism are demonstrated by dual tuning of the geometric and electronic structures, which manifests as a geometric deviation from a honeycomb to an orthorhombic-like structure and formation of P-p_y bonding (P-p_z nonbonding) from P-p_z nonbonding (P-p_y antibonding) because of the increase of the proportion of the P-p_y (P-p_z) orbital.

Keywords: phosphorene, black phosphorus nanostructures, magnetism, Wilson transition, strain effect

(Some figures may appear in colour only in the online journal)

1. Introduction

Recently, exfoliation of black phosphorus [1, 2] into few-layer phosphorene structures has attracted much attention [3–10] because of the distinctive properties of phosphorene nanostructures, such as a moderate direct band gap (∼1.5 eV) [2, 4, 5], high carrier mobility, and large on/off ratio [1–4]. Edge modification and straining are effective approaches used to tailor the electronic and magnetic properties of two-dimensional (2D) monolayer materials [5, 8, 11–16]. For instance, half-metallicity can be achieved by edge modification [14], and the magnetic coupling can be modulated by applying strain to the zigzag graphene nanoribbons (ZGNRs) [15]. Inspired by these strategies, a few studies have attempted to tune the magnetism of PNRs, but stable magnetism has been difficult to achieve on zigzag-PNRs (z-PNRs) and armchair-PNRs (a-PNRs) [16–25]. O-saturated z-PNRs are only spin-polarized in their fixed structures. The unstable magnetism readily disappears by complete relaxation because of edge reconstruction or Peierls distortion [21, 22]. Even in the most recent investigation, magnetism could be achieved on relatively wide (>2 nm) pristine z-PNRs by weakening the

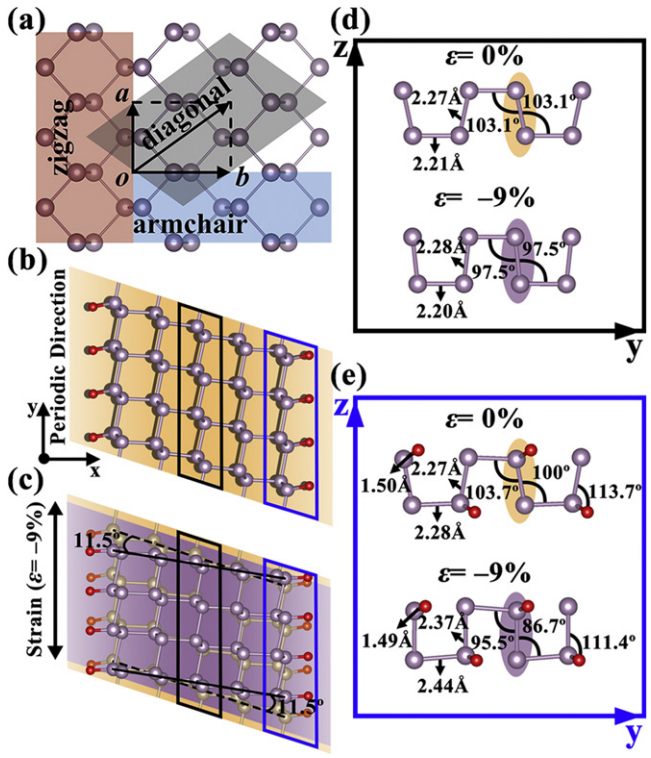

Figure 1. (a) Top view of phosphorene. $\overrightarrow{oa}$ and $\overrightarrow{ob}$ indicate the primitive vectors. The red, blue and grey shaded regions indicate the z-, a-, and d-PNRs, respectively. (b) Structure of AFM0 ($\varepsilon = 0\%$) of O-d-PNR, with the orange shaded area indicating the cell. (c) Structure of NM ($\varepsilon = -9\%$, purple) compared with AFM0 ($\varepsilon = 0\%$, yellow). (d) Differences of P–P bond lengths and P–P–P angles between NM ($\varepsilon = -9\%$) and AFM0 ($\varepsilon = 0\%$) at the center of the O-d-PNRs. (e) The same as (d) but at the edges.

Peierls distortion [23]. However, even in wide pristine z-PNRs, there are still considerable distortions because of the edge interactions of dangling bonds [22, 24]. Thus, achieving stable magnetism in PNRs is still a challenging task.

The fundamental issue is related to the unstable edges. Inspired by two H atom–saturated ZGNRs that simultaneously stabilize the ferromagnetic (FM) edges [26, 27], we propose the idea that the system might realize stable spin-polarization by changing the directions of the dangling bonds of the PNRs. Diagonal PNRs (d-PNRs) constructed by cutting phosphorene along the [110] direction (figure 1(a)) only show alternating up and down dangling bonds at the edges (figure 1(b)). This peculiar ordering of dangling bonds eliminates both of the disadvantages of z/a-PNRs, and thus weakens the coupling interactions between the edges. As is well known, the edge geometric, electronic and magnetic properties, especially the energy bands adjacent to the Fermi level, are highly sensitive to orbital coupling, and the orbital interactions strongly depend on the amount of strain [28, 29]. Previous reports have shown that only O-saturated z-PNRs induce AFM characteristics in their metastable systems, while other elements, such as F, H and S, do not induce spin-polarized properties in PNRs [25]. It is therefore expected that O-d-PNRs could enhance the stability of the edges and versatile electronic and magnetic properties could be achieved by strain modulation.

Here, we focus on the magnetic coupling and evolution of O-d-PNRs with the effect of strain, and realize stable spin-polarized AFM coupling on fully relaxed O-d-PNRs even with a relatively narrow width. AFM coupling is quite stable under both expansive and limited compressive strain. We also find that the irreversible Wilson transition occurs in the process of straining, and surprisingly the derived NM metal phase becomes anomalously more stable than the AFM state, which can be explained by dual tuning of the electronic and geometric transitions: the stability of the resulting metal phase is dramatically enhanced by lowering the energies of the nonbonding and antibonding orbitals to bonding and nonbonding states, respectively, and by the geometric deviation from a honeycomb to an orthorhombic-like structure.

2. Methods

All of the calculations are performed with the Vienna *ab initio* simulation package [30] using density functional theory [31]. The projector augmented-wave method [32, 33] was used to treat the ion–electron interactions, and the Perdew–Burke–Ernzerhof functional [34] was used to describe the exchange–correlation interaction of electrons. The hybrid HSE06 method [35] was used to precisely describe the band structures of the O-d-PNRs. The cutoff energy of the plane-wave basis was set to 500 eV and a $1 \times 5 \times 1$ k-point mesh was used for Brillouin zone integration for the O-d-PNRs. The optimized lattice parameters of phosphorene were $a = 3.31$ Å and $b = 4.57$ Å, which are in good agreement with previous calculations [2, 4, 13]. The d-PNRs shown to present the results are ~12 Å wide (with two repeating cells along the ribbon direction). To eliminate the coupling between neighboring cells, the edge-to-edge and layer-to-layer distances between adjacent d-PNRs were 30 and 15 Å, respectively. A strain $\varepsilon = (d - d_0)/d_0$ was applied along the nanoribbon direction. Under different strains, the structures of the O-d-PNRs were fully relaxed until the force on each atom was less than 0.01 eV Å^{-1} and the energy convergence criteria for electronic iterations was set to be 10^{-5} eV. In addition, the accuracy of the present calculation was checked by calculating the formation energies of d-PNRs with different width.

3. Results and discussion

We first investigated the stability of pristine d-PNRs by comparing the formation energy with the formation energies of z- and a-PNRs with similar widths. The formation energy is defined as $E_f = (E_{pristine} - N_p E_p)/N_p$, where $E_{pristine}$ is the energy of the pristine PNR, N_p is the number of P atoms, and E_p is the energy per atom of phosphorene. The calculated E_f values were 0.14, 0.21, and 0.25 eV for z-, d-, and a-PNRs, respectively, indicating that the stability of the d-PNR is comparable with that of z- and a-PNRs. This trend is in line with the trend of the average dangling bond energies.

Table 1. Relative energies of NM, FM, AFM1, AFM2, and AFM0 ($\varepsilon = 0\%$).

Magnetic phase	Magnetic ordering Edge 1	Edge 2	Energy (meV)
NM			245
FM	↑ ↑ ↑ ↑	↑ ↑ ↑ ↑	72
AFM0	↑ ↑ ↑ ↑	↓ ↓ ↓ ↓	0
AFM1	↑ ↓ ↑ ↓	↓ ↑ ↓ ↑	18
AFM2	↓ ↓ ↑ ↑	↑ ↑ ↓ ↓	9

Naturally, the binding energy of O atoms with d-PNR is given by $E_b = (E_{total} - E_{pristine} - N_O E_O)/N_O$, where E_{total} is the energy of the O-saturated d-PNR, N_O is the number of saturated O atoms, and E_O is the energy of an isolated spin-polarized O atom. The calculated E_b was −5.65 eV, which is slightly lower than the binding energy of O_2. This indicates that the pristine d-PNRs are highly reactive and prone to binding with O atoms but not O_2 molecules, forming rather stable O-d-PNR nanostructures (the stability of the compressed O-d-PNRs will be shown in detail in figure 4). This phenomenon can be easily explained: the dangling bonds at the edges of d-PNRs are alternately arranged up and down. This weakens the repulsive interactions between dangling bonds and facilitates binding with saturated O atoms, which stabilizes the system.

Next, we investigated the electronic and magnetic properties of the fully relaxed O-d-PNRs. This is helpful to understand the following discussion on the strain effect. The magnetic ordering on the same edge is expressed as ↑ and ↓, namely, spin up and spin down, respectively. FM, NM, and all of the AFM phases were considered (in fact, only AFM0, AFM1, and AFM2 have relatively low energies and are listed), and the results are summarized in table 1. AFM0 is the most energetically favorable phase, and FM and NM have 72 and 245 meV higher formation energies, respectively. Moreover, the energy differences among the AFMs are relatively small, facilitating the transitions between them by strain modulation. These will be discussed in detail below. The spin charge density difference ($\rho\uparrow - \rho\downarrow$) of AFM0 is also shown in the inset of figure 2, from which we can clearly see that the magnetic moment is largely localized on the saturated O and binding P atoms at the edges. Furthermore, the O-d-PNRs exhibit FM ordering on the same edge but AFM coupling between two edges. These findings are in line with the case of metastable O-z-PNRs [21]. The origin of the spin-polarized phenomenon of O-d-PNRs can be attributed to the unique dangling bond arrangement at the edges of d-PNRs. This is verified by the fact that the pristine d-PNRs also exhibit AFM character according to our calculations. Such a unique dangling bond arrangement at the edges weakens the interactions between them and facilitates stabilization of the system.

Here, it is worth noting that there is no spin polarization in two-hydrogen saturated edges because of the weak interactions between H and P atoms, whereas O-d-PNRs exhibit spin-polarization in the fully relaxed structures even with a relatively narrow width. On the contrary, O-z-PNRs do not show spin-polarization in their fully relaxed structures [21].

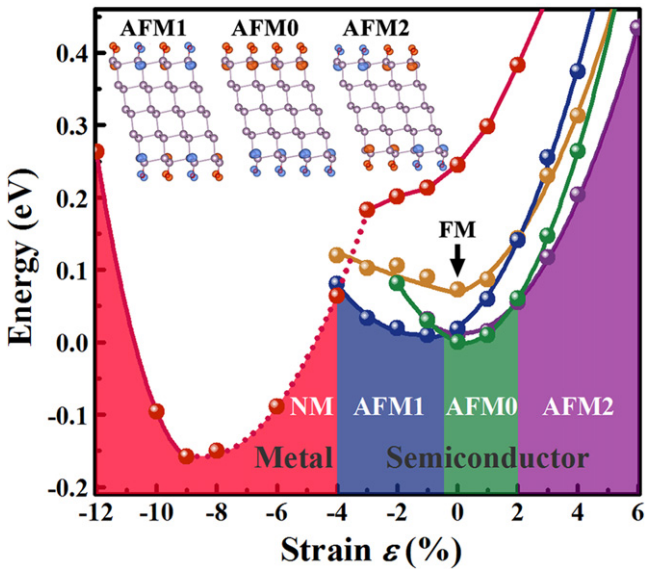

Figure 2. Total energies of the different phases as a function of ε, taking the energy of AFM0 ($\varepsilon = 0\%$) as zero. FM, AFM0, AFM1, AFM2, and NM are presented with the filled areas denoting the most stable phase under the particular range of ε. The spin charge density differences ($\rho\uparrow - \rho\downarrow$) of AFM0, AFM1, and AFM2 are shown in the inset with the different spins distinguished by red (spin-up) and blue (spin-down).

To further understand the spin-polarization phenomenon of the stable AFM0 phase, the spin-polarized band structure is shown in figure 3(a). The O-d-PNRs exhibit semiconductor properties with an indirect band gap (~1.07 eV), and the magnetism arises from the eight spin-polarized bands adjacent to the Fermi level because of the incompletely saturated O–P bonds. Because O is more electronegative than P, it withdraws electrons from the P atoms. According to the Bader charge analysis [36], each O accepts an average of about 1.8 electrons from the d-PNRs, but each dangling bond only provides 1.0 electron. Consequently, magnetism can be found at both the edges of the d-PNRs and the saturated O atoms based on the weakened interactions of the edges.

The partial charge densities of the selected bands adjacent to the Fermi level of AFM0 are shown in figure 3(a), namely, VB1, VB2, and CB. Combined with the projected electronic wave functions on the different atomic orbitals, both VB2 and CB are mainly composed of the dominant nonbonding P-p_z orbital with a small proportion of the P-p_y state at the edges along the nanoribbon direction. VB1 shows a mixed character of antibonding P-p_y and P-p_z states at the edges with a relatively large proportion of the P-p_y component.

In the following, under the effect of ε, the constituents of VB1, VB2 and CB dramatically change. This modification plays a decisive role in stabilizing the transition system, i.e. from the semiconductor to the metal phase.

We now focus on strain modulation of the electronic and magnetic properties of O-d-PNRs. Strain was applied along the nanoribbon direction in the range −12 to 6% (see

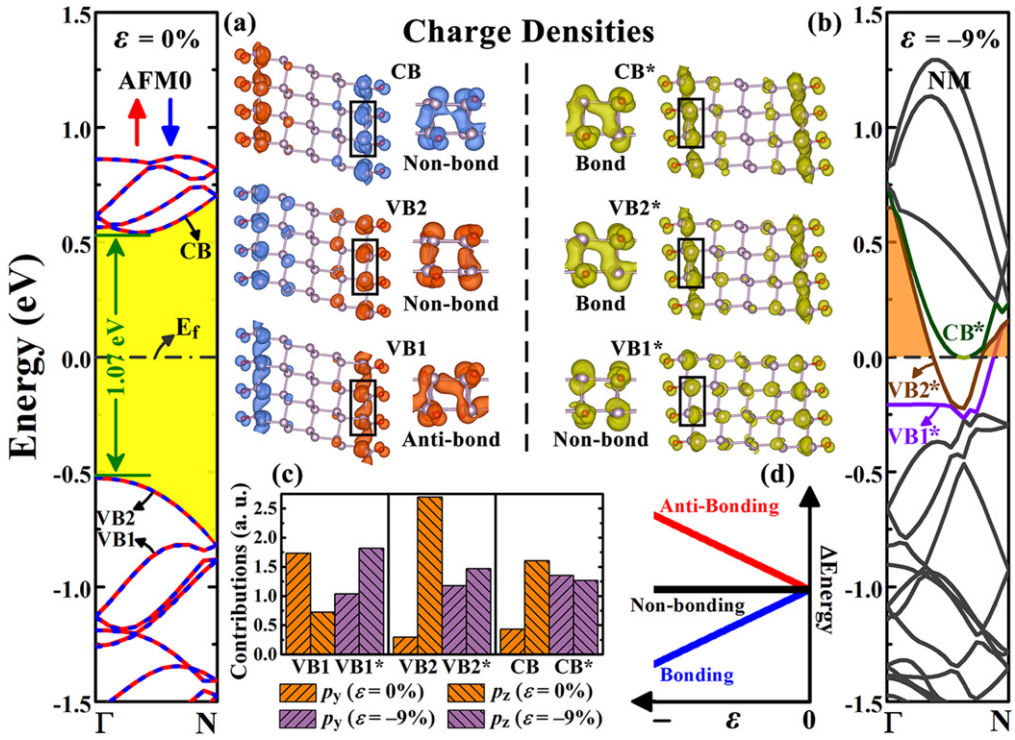

Figure 3. (a) Band structure of AFM0 ($\varepsilon = 0\%$) with spin-up and spin-down indicated by red and blue, respectively. The partial charge densities (top and side views) including spin-up (red) and spin-down (blue) bands of VB1, VB2, and CB are also shown. (b) Band structure of NM ($\varepsilon = -9\%$) with VB1*, VB2*, and CB* corresponding to the same band number of VB1, VB2 and CB, respectively. (c) Comparison of the proportions of the contributions of the P-p_z and P-p_y orbitals for NM and AFM0. (d) Schematic diagram of the energy response to compressive strain for anti-bonding, non-bonding, and bonding states.

figure 2). Magnetic evolution can be seen from the total energies of all of the magnetic phases as a function of ε. Specifically, the O-d-PNRs exhibit the AFM0 phase when ε is in the range −0.5 to 2%. When the compressive strain is in the range $-4\% < \varepsilon < -0.5\%$, the system exhibits the AFM1 phase. In contrast, when the expansive strain exceeds 2%, the AFM2 state is found to be energically favorable. The fully relaxed AFM0 phase with no strain is the most stable state in the range −4 to 6%. By comparing the magnetic orderings of the AFM0, AFM1, and AFM2 phases (see the inset of figure 2), it is evident that in the process of magnetic evolution, the magnetic moment on the same edge of the O-d-PNR transforms from FM to AFM ordering. However, AFM coupling between two opposite edges is quite steady regardless of the magnetic variations at the edges because of the interference effect of the magnetic tails derived from the two edges, as mentioned above. In addition, a semiconductor character is retained throughout the range −4 to 6%.

It should be emphasized that the Wilson transition from semiconductor (AFM) to metal (NM) occurs very naturally when the applied compressive strain exceeds −4%, but more surprisingly and anomalously, the NM phase has the lowest energy when $\varepsilon = -9\%$. In other words, the NM phase becomes the new ground state of the O-d-PNR because its energy is lower than AFM0. Moreover, such a Wilson transition is irreversible because the energy barrier of the reverse transition is high (~0.22 eV).

To explain the mechanism of the Wilson transition and the new ground state of NM, we first address the geometric changes of O-d-PNRs by strain modulation. The geometric structures of AFM0 ($\varepsilon = 0\%$) and NM ($\varepsilon = -9\%$) are shown in figures 1(b) and (c). Evidently, a compressive strain of −9% induces a shear deformation (~11.5°) perpendicular to the nanoribbon direction of the O-d-PNR in contrast to $\varepsilon = 0\%$. This shear stress changes AFM0 from a honeycomb to a NM orthorhombic-like structure, as indicated by the P–P bonds at both the edges and the center of the O-d-PNRs and the O–P bonds becoming nearly perpendicular to each other (see figure 1(d) and (e)). At the edges, the average angle between O and the edge P decreases from 113.7° to 111.4°, whereas the changes in the average P–P bond length and P–P–P bond angle are more apparent, with the bond length increasing by ~0.1 Å and the bond angle decreasing by ~10°. These changes are also found at the center of the O-d-PNRs.

Such a significant geometric distortion undoubtedly affects the electronic properties. Figure 3(b) shows the band structure of the NM phase under $\varepsilon = -9\%$. The metal character derived from the Wilson transition is explicitly verified by the three bands crossing the Fermi level, namely, VB1*, VB2*, and CB*. These three bands correspond to the same band number of VB1, VB2, and CB in AFM0. As the Wilson transition occurs, VB1* and VB2* shift upward while CB* simultaneously shifts downward across the Fermi Level. To more deeply investigate the stabilization mechanism of the

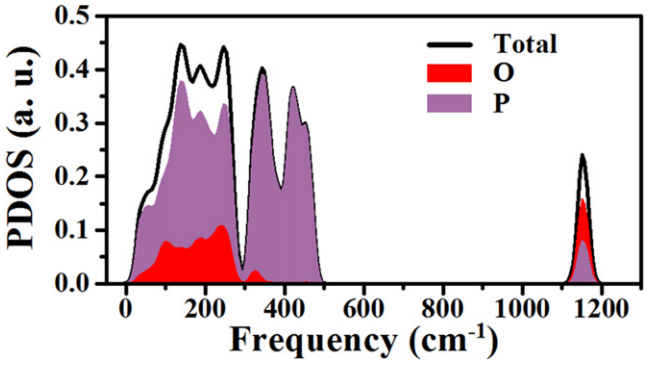

Figure 4. Total and partial PDOS of NM ($\varepsilon = -9\%$).

metal phase, the partial charge densities of the three bands are also plotted with that of AFM0 for comparison. For CB* and VB2*, enhanced bonding properties are present along the nanoribbon direction. This is manifested by the formation of the P-p_y bonding character in NM from the previous P-p_z nonbonding state in AFM0 because of the increase of the proportion of the P-p_y orbital (see figure 3(c)). For VB1*, the P-p_z nonbonding property is derived from the P-p_y antibonding state by increasing the proportion of the P-p_z component. The stability of the derived metal phase under $\varepsilon = -9\%$ is considerably enhanced by a combination of lowering the energies of the nonbonding orbitals CB and VB2 as well as the antibonding orbital VB1 (see figure 3(d)). Here, we should note that both the geometric distortion and the electronic transition contribute to the stabilization of the metal phase.

To further verify the stability of the metallic characteristics of O-d-PNRs, the phonon density of states (PDOS) were calculated using the PHONOPY software [37]. Figure 4 shows the total and partial PDOS of NM ($\varepsilon = -9\%$). Clearly, no imaginary frequencies emerged, confirming the dynamical stability of the metal phase. Both the low-frequency ($<300\,\mathrm{cm}^{-1}$) and high-frequency ($1100–1200\,\mathrm{cm}^{-1}$) regions can be attributed to the vibrations of O and P atoms, while the medium-frequency region is almost completely composed of P atoms. It is noteworthy that if the zero-point vibration energies are taken into consideration, there is no significant change for the energy difference between NM ($\varepsilon = -9\%$) and AFM0 ($\varepsilon = 0\%$) ~0.22 eV, which again verifies the structural stability of the derived metal system.

4. Conclusions

In summary, we have presented a detailed study of the magnetic evolution and strain effect on O-d-PNRs. The fully relaxed O-d-PNRs exhibit spin-polarized antiferromagnetic (AFM) coupling, which is quite stable under expansive and limited compressive strains. We also find that the irreversible Wilson transition occurs for $\varepsilon < -4\%$. More importantly, the resulting metal phase becomes anomalously more stable than the AFM under axial compressive strain. The related stabilization mechanism is investigated in detail, and can be attributed to the dual tuning of the electronic and geometric transitions: the stability of the derived metal phase is considerably enhanced by the lowering of the energy levels of the nonbonding orbitals CB and VB2 as well as the antibonding orbital VB1, and also by the geometric deviation from a honeycomb to an orthorhombic-like structure. These findings are expected to play an important role in the future design of functional phosphorene nanoelectronic devices.

Acknowledgments

Yu Jia and Chong Li gratefully acknowledge projects funded by the National Basic Research Program of China (grant no. 2012CB921300), the National Natural Science Foundation of China (grant nos. 11274280 and 11304288), the Postdoctoral Science Foundation of China and Henan Province (grant nos. 2014M552009 and 2013001), and the Development Foundation for Outstanding Young Teachers of Zhengzhou University (ZZU) (grant no. 1421317051). W S Su would like to thank the National Science Council of Taiwan for financially supporting this research under contract no. NSC-101-2112-M-492-001-MY3. The calculations were performed at the High Performance Computational Center of ZZU.

References

[1] Li L, Yu Y, Ye G J, Ge Q, Ou X, Wu H, Feng D, Chen X H and Zhang Y 2014 Black phosphorus field-effect transistors *Nat. Nanotechnology* **9** 372
[2] Liu H, Neal A T, Zhu Z, Luo Z, Xu X, Tománek D and Ye P D 2014 Phosphorene: an unexplored 2D semiconductor with a high hole mobility *ACS Nano* **8** 4033
[3] Xia F, Wang H and Jia Y 2014 Rediscovering black phosphorus as an anisotropic layered material for optoelectronics and electronics *Nat. Commun.* **5** 4458
[4] Qiao J, Kong X, Hu Z-X, Yang F and Ji W 2014 High-mobility transport anisotropy and linear dichroism in few-layer black phosphorus *Nat. Commun.* **5** 4475
[5] Rodin A S, Carvalho A and Castro Neto A H 2014 Strain-induced gap modification in black phosphorus *Phys. Rev. Lett.* **112** 176801
[6] Wei Q and Peng X 2014 Superior mechanical flexibility of phosphorene and few-layer black phosphorus *Appl. Phys. Lett.* **104** 251915
[7] Guan J, Zhu Z and Tománek D 2014 Tilling phosphorene *ACS Nano* **8** 12763
[8] Fei R and Yang L 2014 Strain-engineering the anisotropic electrical conductance of few-layer black phosphorus *Nano Lett.* **14** 2884
[9] Jing Y, Tang Q, He P, Zhou Z and Shen P 2015 Small molecules make big differences: molecular doping effects on electronic and optical properties of phosphorene *Nanotechnology* **26** 095201
[10] Liu Q, Zhang X, Abdalla L B, Fazzio A and Zunger A 2015 Switching a normal insulator into a topological insulator via electric field with application to phosphorene *Nano Lett.* **15** 1222
[11] Ziletti A, Carvalho A, Campbell D K, Coker D F and Castro Neto A H 2015 Oxygen defects in phosphorene *Phys. Rev. Lett.* **114** 046801

[12] Ge Y, Wan W, Yang F and Yao Y 2015 The strain effects on superconductivity in phosphorene: a first-principles prediction *New J. Phys.* **17** 035008
[13] Peng X, Wei Q and Copple A 2014 Strain-engineered direct-indirect band gap transition and its mechanism in two-dimensional phosphorene *Phys. Rev.* B **90** 085402
[14] Kan E-J, Li Z, Yang J and Hou J G 2008 Half-metallicity in edge-modified zigzag graphene nanoribbons *J. Am. Chem. Soc.* **130** 4224
[15] Hu T, Zhou J, Dong J and Kawazoe Y 2012 Strain-induced ferromagnetism in zigzag edge graphene nanoribbon with a topological line defect *Phys. Rev.* B **86** 125420
[16] Guo H, Lu N, Dai J, Wu X and Zeng X C 2014 Phosphorene nanoribbons, phosphorus nanotubes, and van der Waals multilayers *J. Phys. Chem.* C **118** 14051
[17] Zhang J, Liu H J, Cheng L, Wei J, Liang J H, Fan D D, Shi J, Tang X F and Zhang Q J 2014 Phosphorene nanoribbons as a promising candidate for thermoelectric applications *Sci. Rep.* **4** 6452
[18] Li W, Zhang G and Zhang Y-W 2014 Electronic properties of edge-hydrogenated phosphorene nanoribbons: a first-principles study *J. Phys. Chem.* C **118** 22368
[19] Liang L, Wang J, Lin W, Sumpter B G, Meunier V and Pan M 2014 Electronic bandgap and edge reconstruction in phosphorene materials *Nano Lett.* **14** 6400
[20] Han X, Stewart H M, Shevlin S A, Catlow C R A and Guo Z X 2014 Strain and orientation modulated bandgaps and effective masses of phosphorene nanoribbons *Nano Lett.* **14** 4607
[21] Zhu Z, Li C, Yu W, Chang D, Sun Q and Jia Y 2014 Magnetism of zigzag edge phosphorene nanoribbons *Appl. Phys. Lett.* **105** 113105
[22] Maity A, Singh A and Sen P 2014 Peierls transition and edge reconstruction in phosphorus nanoribbons arXiv:1404.2469v2
[23] Du Y, Liu H, Xu B, Sheng L, Yin J, Duan C-G and Wan X 2014 Tunable magnetic semiconductor behavior driven by half-filled one dimensional band in zigzag phosphorene nanoribbons arXiv:1409.4134
[24] Ramasubramaniam A and Muniz A R 2014 *Ab initio* studies of thermodynamic and electronic properties of phosphorene nanoribbons *Phys. Rev.* B **90** 085424
[25] Peng X, Copple A and Wei Q 2014 Edge effects on the electronic properties of phosphorene nanoribbons *J. Appl. Phys.* **116** 144301
[26] Son Y-W, Cohen M L and Louie S G 2006 Energy gaps in graphene nanoribbons *Phys. Rev. Lett.* **97** 216803
[27] Lee H, Son Y-W, Park N, Han S and Yu J 2005 Magnetic ordering at the edges of graphitic fragments: magnetic tails interactions between the edge-localized states *Phys. Rev.* B **72** 174431
[28] Cheng Y C, Wang H T, Zhu Z Y, Han Y, Zhang X X and Schwingenschlögl U 2012 Strain-activated edge reconstruction of graphene nanoribbons *Phys. Rev.* B **85** 073406
[29] Cheng Y C, Zhu Z Y and Schwingenschlögl U 2012 Mechanical failure of zigzag graphene nanoribbons under tensile strain induced by edge reconstruction *J. Mater. Chem.* **22** 24676
[30] Kresse G and Furthmüller J 1996 Efficient iterative schemes for *ab initio* total-energy calculations using a plane-wave basis set *Phys. Rev.* B **54** 11169
[31] Kohn W and Sham L J 1965 Self-consistent equations inducing exchange and correlation effects *Phys. Rev.* **140** A1133
[32] Blöchl P E 1994 Projector augmented-wave method *Phys. Rev.* B **50** 17953
[33] Kresse G and Joubert D 1999 From ultrasoft pseudopotentials to the projector augmented-wave method *Phys. Rev.* B **59** 1758
[34] Perdew J P, Burke K and Ernzerhof M 1996 Generalized gradient approximation made simple *Phys. Rev. Lett.* **77** 3865
[35] Heyd J, Scuseria G E and Ernzerhof M 2003 Hybrid functionals based on a screened Coulomb potential *J. Chem. Phys.* **118** 8207
Heyd J, Scuseria G E and Ernzerhof M 2006 *J. Chem. Phys.* **124** 219906 (erratum)
[36] Henkelman G, Arnaldsson A and Jónsson H 2006 A fast and robust algorithm for Bader decomposition of charge density *Comput. Mater. Sci.* **36** 354
[37] Togo A, Oba F and Tanaka I 2008 First-principles calculations of the ferroelastic transition between rutile-type and $CaCl_2$-type SiO_2 at high pressures *Phys. Rev.* B **78** 134106